Detection of colorless plastic contaminants hidden in cotton layer using chromatic polarization imaging

Bo Peng (彭 波)*, Shaling Huang (黄莎玲), and Dongjie Li (李东杰)

Institute of Electronic Engineering, China Academy of Engineering Physics, Mianyang 621900, China
**Corresponding author: pengb07@gmail.com*

Received April 25, 2015; accepted June 30, 2015; posted online August 5, 2015

A method of chromatic polarization imaging is presented for the online detection of colorless plastic contaminants from ginned cotton in an industrial setting. To understand the experimental results, we consider a realistic microscopic model, including the multiple scattering of anisotropic fibers and the light propagation in anisotropic slabs. A Monte Carlo code, based on the extended Jones matrix, is developed to simulate photon migration with polarization states, and phase information followed. Using simulations and experiments, we analyze the underlying mechanisms and evaluate the performance of this method with different layer thicknesses. Our approaches proposed in this Letter also have the potential to be applied in tissue imaging, remote sensing, and other scenarios.

OCIS codes: 290.5839, 290.5855, 290.7050, 290.5850.
doi: 10.3788/COL201513.092901.

In the textile industry, plastic contaminants such as shopping bags, weaving tapes, and agricultural mulching films are inevitably mixed into ginned cotton during picking, transportation, and other processes[1]. Great progress has been made recently with various methods, e. g., near-infrared identification[2], multispectral imaging[1,3], fluorescence detection[4] and a multitude of image recognition algorithms[5–7], to pick out colored and/or fluorescent plastic contaminants in real time. Unfortunately, colorless contaminants still remain invisible to the methods above, especially when they are hidden in the cotton layer. Therefore, the online detection of these colorless plastic contaminants continues to be a serious challenge for the textile industry worldwide.

After an initial analysis, we found that these contaminants hidden in the cotton layer characterize the anisotropic structure, and are a result of the plastic molding in the industrial manufacturing or the mechanical stretching in the cotton ginning. It is well known that anisotropic objects can produce the chromatic polarization (CP) phenomenon, which is an interference effect when placed between crossed polarizers with white light shining. Therefore, we expect to utilize this phenomenon to distinguish the contaminants from the cotton. Unfortunately, cotton fibers have the same features. In general, the bright CP colors of cotton fibers are used to identify their maturity[8]. Thus, the question arises whether one can effectively detect colorless plastic contaminants from the cotton layer by using a real-time CP imaging method.

To explore if this method is effective or not, we conducted an experiment in which a polypropylene weaving tape (a type of common contaminant) and a 5 mm-thick cotton layer were used as samples. As shown in Fig. 1(a), due to its colorless and transparent nature, the weaving tape is almost invisible to our eyes, even when it is placed on the layer's surface. Thus, we depicted its contour with a black dotted line in Fig. 1(a), and showed the clear appearance of its surface glossiness on a black background in the inset. Clearly, the cotton layer sample in our experiment forms an opaque "wall," completely obscuring the 2 mm-squared background grid. In the measurements, the CP images of the cotton fiber and the weaving tape were first observed using a polarizing microscope with different magnifications [see Figs. 1(b) and 1(c), respectively]. Note that, to demonstrate the validity of our method, we particularly selected cotton fibers and weaving tape with similar CP colors. In fact, owing to the differences in their own anisotropy, cotton fibers and weaving tapes generally have distinct CP colors.

In our sample, the fiber's diameter is approximately 6 μm, while the width of the weaving tape is 2.5 mm. The experimental scheme is illustrated in Fig. 1(d), with a white light-emitting diode (w-LED) serving as a light source. On the left of Fig. 1(d) is the spectral curve of the

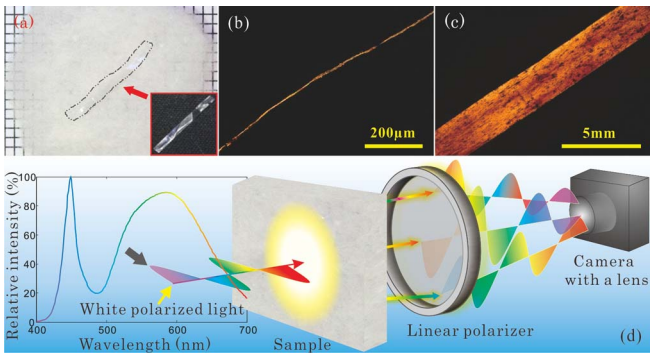

Fig. 1. Schematic diagram of the CP imaging method. (a) The colorless weaving tape placed on a 5 mm-thick cotton layer; (b) and (c) polarized light microscopy of a single cotton fiber and the tape, respectively. (d) Scheme of the experimental setup.

w-LED measured with a spectrometer (Zolix Omni-λ300). Travelling in turn through a lens, an aperture, and a linear polarizer (not shown here), a beam from the w-LED yields the collimated white polarized light and then is normally incident on the surface of the sample [see Fig. 1(d)]. The incident beam produced a diffused speckle pattern on the sample and is transmitted through it in different directions. Another linear polarizer, whose polarization is perpendicular to the first one, is used to analyze the transmitted light. To record the CP images of the sample, a CCD camera equipped with a zoom lens is placed ~15 cm away, behind the second linear polarizer.

Figure 2 shows the experimental images. Contrary to the CP image of the tape [see Fig. 2(a)], the cotton layer appears to be different colors from those fibers inside it, as illustrated in Fig. 2(b). Indeed, the CP colors of the layer on the wide field are a composite of various colored fiber fractions [see the enlarged view in the inset of Fig. 2(b)]. With a careful analysis, we found that the subtle phenomenon not only resulted from the CP of the fibers' anisotropy, but also from the light scattering due to their small size. In short, the above phenomenon seen in the cotton layer is caused by multiple scattering from a large number of randomly oriented anisotropic fibers. Figure 2(c) shows the CP image of the weaving tape covered by the cotton layer. Surprisingly, the tape can be clearly identified even when it is hidden beneath the layer, but it is invisible in its transmission image [see Fig. 2(d)]. Our results prove that colorless plastic contaminants can be effectively detected in the cotton layer by using the CP imaging.

However, it is not clear yet why the contaminants, which are completely buried in the cotton layer, can keep their CP features. The phase information of photons, beyond all questions, must be impaired by the scattering of the fibers. Thus, is this phenomenon in our sample only dependent on the unscattered photons? Actually, these problems are involved in polarized light propagation in the scattering medium, which is composed of both anisotropic fibers and anisotropic slabs. To our knowledge, the propagation of polarized light into scattering media can be modeled using statistical methods, such as the Monte Carlo simulation with a Stokes or Jones formalism[9–11]. Currently, more than 1000 Monte Carlo codes have been specially developed for various applications ranging from the life sciences to atmospheric optics[12–18]. Here, to explore the phase evolution and the polarization altering of photons during their propagation, we developed a Monte Carlo simulation that is based on an extended Jones matrix.

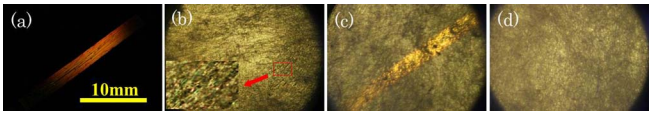

Fig. 2. (a) Experimental CP images of colorless weaving tape, (b) cotton layer and (c) their mixture where the tape is placed beneath the layer. In contrast to (c), a transmission image (d) was captured with the second linear polarizer removed.

Concretely, this simulation is implemented with a realistic medium model, which accounts for the microstructure of the sample used in our experiments (see Fig. 3). The model consists of both anisotropic fibers and anisotropic contaminants. The length of the fibers can be approximated by their extremely long anisotropic cylinders due to their large ratio of length to diameter, while the contaminants are compared to uniaxial slabs on account of their film-like appearance and stretch-induced anisotropy. As illustrated in Fig. 3(a), the fates of the photons passing through the horizontal linear polarizer (H) are either scattered by the fibers or interact with the contaminants. To characterize the fibers' scattering, we employed a formalism based on an extended Jones matrix[19], in which the scattering regime of an anisotropic cylinder with polarized photons illuminating at oblique incidence is introduced. Scattered off the cylinder, the photons form a cone with half angle relative to the axis equaling to the incident angle ζ [see Fig. 3(b)]. Details about this regime have been described in our previous work[20] (here, the misprints of Eqs. (3) and (4) in Ref. [20] are corrected by exchanging the minor diagonal components J_3 and J_4 of the Jones matrix, and another misprint below Eq. (1) is $\xi_{\pm} = a \cdot \chi_{\pm}$). In our simulation, two orthogonal components (indicated by the subscripts p and s) of the electric field are introduced to express the photon's Jones vectors for characterizing its polarization state and phase shift. Going through N scattering events, the Jones vector of a scattered photon can be written in matrix form as follows:

$$\begin{pmatrix} E_p^s \\ E_s^s \end{pmatrix} = \left[\prod_{i=1}^{N} \mathbf{J}(\zeta_i, \phi_i)\mathbf{T}(\alpha_i)\mathbf{P}(s_i)\right]\begin{pmatrix} E_p^i \\ E_s^i \end{pmatrix}, \quad (1)$$

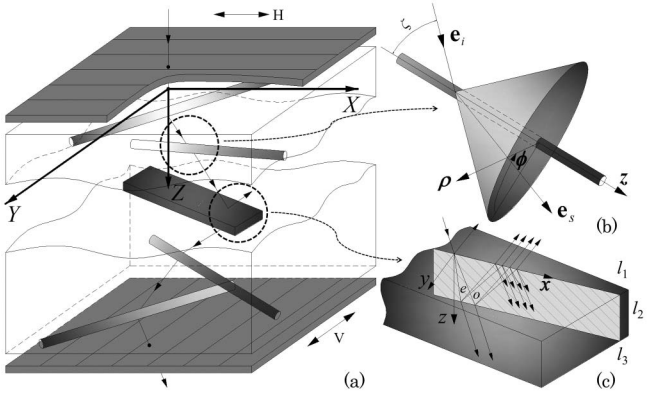

Fig. 3. Schema of photon propagation in the fiber-contaminant mixture. (a) A realistic microscopic model, in which the above and beneath elements are two crossed polarizers, H and V, respectively. (b) Single scattering of oblique incident light by an anisotropic fiber in a cylindrical coordinate system $p\phi z$. (c) Photon migration of birefringence and multiple bireflectances within the contaminant denoted in a local frame xyz.

where $\mathbf{J}(\zeta_i, \phi_i)$ is the single-scattering Jones matrix described by Eq. (4) in Ref. [20], $\mathbf{T}(\alpha_i)$ is a 2×2 rotational matrix, and α_i is the angle between the incident plane and the p-component of the photon's Jones vector in the ith scattering event. $\mathbf{P}(s_i) = [\exp(jkn_o s_i)0; 0\ \exp(jkn_e(w)s_i)]$ is the phase retardation matrix of the photon migrating in the isotropic surrounding medium (air), whose parameter s_i is the migration distance of the photon after the previous scattering, and the superscripts i and s in the Jones vectors denote the incident and the scattered photon, respectively.

When the photon hits the contaminant, the cause is apparently either the reflection or the transmission. As shown in Fig. 3(c), due to the contaminant's anisotropy, birefringence and bireflectance generally happen inside of it, where the photon is split into o and e waves. To explore the interactions of the incident photon with the contaminant, we calculated the electric field amplitude coefficients and the propagation directions of the photon when it impinged onto a uniaxial slab with the optical axis oriented arbitrarily. In detail, the amplitude coefficients of the reflection and the transmission can be calculated based on the modal decomposition and the boundary conditions of electromagnetic field[21], while the propagation directions are based on Huygens' principle[22]. Obviously, it is very complicated to follow the photons' travels in the simulation. Thus, we combined all the photons that exit from the upper or lower surface into a single compound wave, taking into consideration their phase retardations during the migration[23,24]. Using an extended Jones matrix formalism, we can determine the transmitted photons' Jones vector in matrix form as

$$\begin{pmatrix} E_{tp} \\ E_{ts} \end{pmatrix} = (\mathbf{T}_{oe}^{23}\mathbf{P}_{oe}^{+}) \left\{ \sum_{q=0}^{\infty} \begin{bmatrix} (\mathbf{R}_{oe}^{21}\mathbf{P}_{oe}^{-})(\mathbf{R}_{oe}^{23}\mathbf{P}_{oe}^{+}) \\ \times \exp(j\delta^{23}) \end{bmatrix}^q \right\} \mathbf{T}_{ps}^{12} \begin{pmatrix} E_{ip} \\ E_{is} \end{pmatrix}, \tag{2}$$

in which $\mathbf{P}_{oe}^{\pm}$, similar to $\mathbf{P}(s_i)$, is the phase retardation matrix of the o and e waves, and relates to their migration distances during two adjacent interactions with the interface. The "$\pm$" signs in all cases correspond to the propagation direction of waves with respect to the z-axis in the local frame xyz. The superscript numbers in Eq. (2) are used to flag the photon propagation from one medium to another, since the contaminant are labeled as l_2 and sandwiched between two media l_1 and l_3 [see Fig. 3(c)]. $\mathbf{T}_{ps}^{12} = [t_{po}^{12}\ t_{so}^{12}; t_{pe}^{12}\ t_{se}^{12}]$ and $\mathbf{T}_{oe}^{23} = [t_{op}^{23}\, t_{ep}^{23} \exp(j\Delta^{+}); t_{os}^{23}\, t_{es}^{23} \exp(j\Delta^{+})]$ are the transmission matrices of the incident waves p, s and o, e, whose elements consist of the corresponding transmitted coefficients, in which the subscripts represent the conversion from one wave to another, and the phase factor $\exp(j\Delta^{\pm})$, which represents the phase shifts produced by the different incidence points of waves o and e within the contaminant. The phase differences $\Delta^{\pm}$ can be calculated based on the geometric method as shown below:

$$\Delta^{\pm} = khn_o \frac{\sin\theta_o^{\pm}}{\cos\theta_o^{\pm}\cos\theta_e^{\pm}} \sqrt{\cos^2\theta_o^{\pm} + \cos^2\theta_e^{\pm} - 2\cos\psi\cos\theta_o^{\pm}\cos\theta_e^{\pm}}. \tag{3}$$

where k is the wave number of the ambient medium (air), h is the thickness of the contaminant, n_o is the refractive index of o wave, θ_o and θ_e are the angles of refraction of the corresponding waves, and ψ is referred to as the angle between the waves o and e. Similarly, we can get the reflection matrices $\mathbf{R}_{oe}^{21}$ and $\mathbf{R}_{oe}^{23}$. Furthermore, $\delta^{23} = 2kn_o h \tan\theta_o \sin\theta_t$ is an additional phase difference between the two adjacent transmitted waves. Again, in a manner analogous to the transmission case, we can derive the reflected compound wave as follows:

$$\begin{pmatrix} E_{rp} \\ E_{rs} \end{pmatrix} = \left\{ \begin{matrix} (\mathbf{T}_{oe}^{21}\mathbf{P}_{oe}^{-}) \sum_{q=0}^{\infty} \left[\begin{matrix} (\mathbf{R}_{oe}^{23}\mathbf{P}_{oe}^{+})(\mathbf{R}_{oe}^{21}\mathbf{P}_{oe}^{-}) \\ \exp(j\delta^{21}) \end{matrix} \right]^q \\ \times (\mathbf{R}_{oe}^{23}\mathbf{P}_{oe}^{+})\mathbf{T}_{ps}^{12} + \mathbf{R}_{ps}^{12} \end{matrix} \right\} \begin{pmatrix} E_{ip} \\ E_{is} \end{pmatrix}. \tag{4}$$

Now using the above formalism, we implemented an extended Jones matrix-Monte Carlo simulation (EJM-MC). Specifically, we first normalized the spectral intensity distribution of the white polarized light exhibited on the left of Fig. 1(d), and then used the inversion transformation method to sample each photon's wavelength before its launch. Next, we assumed that the fibers in our model are uniformly distributed in the plane parallel to the XY plane and have a Gaussian distribution with a standard deviation 10° in depth (z-axis direction), which accounts for the conglomerated state of our sample. Besides, the optical axis of the contaminant is approximated to be within the plane parallel to the surface, according to its anisotropic structure. When encountering the contaminant, the photon gets one of two possible fates, reflection or transmission, which depends on the ratio of the reflected intensity to the transmitted one. The simulation should not be terminated until all given photons are calculated completely. In order to render the experimental images, we pinned the emergent photons to the specified image grids according to their exit positions, and then calculated the interferences of the photons in each grid based on their wavelengths. Finally, using the International Commission on Illumination color-matching functions[25], we converted the spectral intensity of every grid into the corresponding pixel color of the simulated images.

To evaluate the performances of the transmission and reflection modes, we calculated the relative intensity of a contaminant in both modes and plotted the results in Fig. 4(a), using $I = |\mathbf{E}|^2$ from Eqs. (2) and (4). As for the axial and radial refractive indices of the contaminant, the standard values were used; the values are 1.514 and 1.493, respectively. Besides, the contaminant, in accordance with the sample, leans at 45° relative to the horizontal polarizer. The results indicated that the transmitted intensity was greater than the reflected one, which clearly proved that the former can produce a stronger CP

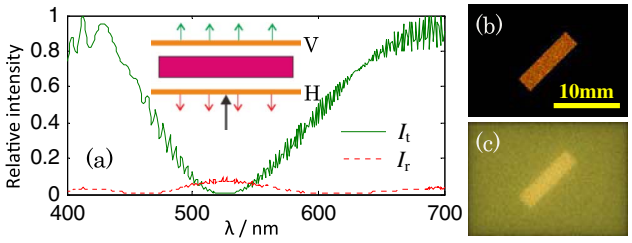

Fig. 4. (a) The relative intensity of the transmission and reflection modes with only a contaminant. (b) and (c) show the simulated CP images of the contaminant uncovered and covered by the cotton layer, respectively.

interference effect than the latter. Therefore, in the CP imaging, we focus our attentions only on the transmission. In Figs. 4(b) and 4(c), we showed the simulated CP images, where the size dimensions of the contaminant are set to 10 mm (length) × 2.5 mm (width) × 50 μm (thickness), and the cotton layer is 5 mm in thickness, with a concentration of 50 mm^{-2}. The simulation is carried out with 2×10^7 photons followed. By comparison, we found that, to a certain extent, the simulated images bear a resemblance to the experimental ones, whether or not the contaminant covered by the cotton layer. Here, note that the contaminant exhibits some subtle variations in its CP color when sheltered by the layer. Obviously, this is related to the fact that the phase information of the photons is scrambled by the fibers' scattering.

To find out what photons form the CP images of the contaminant, we counted the number of photons that occurred in the image Fig. 4(c) over their scattering number, and showed the corresponding calculated images (see Fig. 5). Without a doubt, not only the unscattered but also the weakly scattered photons ($n \leq 3$) can keep the CP features of the contaminant. Instead, multi-scattered photons ($n \geq 4$) manifest as background noise, due to the loss of information about their phases. However, the contaminant can be clearly distinguished from the image in Fig. 4(c), since the unscattered and the weakly scattered photons play a predominant part in the transmitted light for the 5 mm-thick cotton layer [see Fig. 5(a)]. In order to evaluate the performance of our method, we investigated CP imaging with different layer thicknesses and embedded the contaminants in them, with a 2 mm-thick layer placed at the bottom.

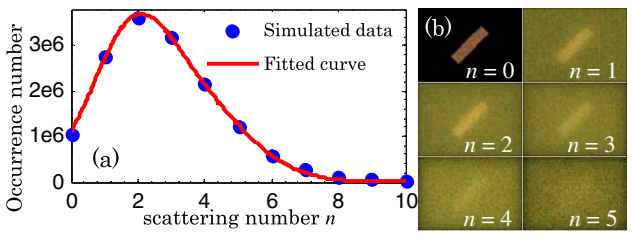

Fig. 5. (a) The occurrences of the photons in the image vs. their scattering number n. (b) Corresponding calculated CP images for different values of n.

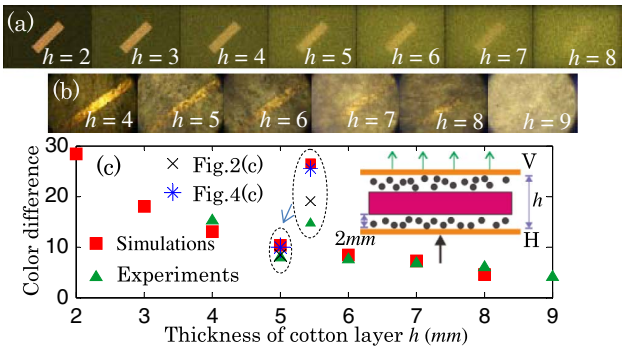

Fig. 6. (a) Simulated and (b) measured images and (c) their contaminants, which are the background color difference over the different layer thicknesses h.

As illustrated in Figs. 6(a) and 6(b), the images of the simulations and experiments show that this method can detect contaminants from about an 8 mm-thick layer, which is beyond the industrial requirement of a 5 mm standard thickness. To assess the visibility of the contaminants on average from the background in these images, we used a color difference method (ΔE_{2000})[26] for objective evaluation. As plotted in Fig. 6(c), the experimental data agree well with the simulated ones, showing an exponential decrease as the layer becomes thicker. By comparing the color differences between Figs. 2(c), 4(c), 6(a), and 6(b) at $h = 5$, we can see that wherever contaminants are buried has no effect on the performance of our method.

In conclusion, we propose a CP imaging method that can be used in real-time detection in the textile industry. To explain the CP features in our initial experiments, we consider a realistic scattering model composed of anisotropic fibers and anisotropic slabs, and then develop a Monte Carlo simulation based on an extended Jones matrix, in which not only the polarization states but the phase information of photons can be followed. The simulated images closely match the measured ones. We then analyze the potential mechanisms and evaluate the performance of this method with different layer thicknesses. The results prove that the detectable thickness (~8 mm) is beyond the industrial requirement (5 mm). So the CP imaging is a simple but effective method for the online detection of colorless plastic contaminants in ginned cotton. The approaches proposed in this Letter also have the potential to characterize the microstructures and simulate the polarized light imaging in both biomedicine and remote sensing[27–30].

This work was supported by the Ministry Fund of China (No. 00404010503-4) and the Innovation Development Fund of IEE CAEP (No. S20141102).

References

1. D. Y. Jia and T. H. Ding, Meas. Sci. Technol. **16**, 1355 (2005).
2. C. A. Fortier, J. E. Rodgers, M. S. Cintron, X. L. Cui, and J. A. Foulk, Text. Res. J. **81**, 230 (2011).

3. J. Guo, Y. Ying, J. Li, X. Rao, Y. Kang, and Z. Shi, Trans. CSAE **28**, 126 (2012).
4. F. Zhou and T. H. Ding, Appl. Spectrosc. **64**, 936 (2010).
5. W. Z. Yang, D. L. Li, L. Zhu, Y. Kang, and F. Li, Comput. Electron. Agric. **68**, 68 (2009).
6. R. H. Ji, D. L. Li, L. R. Chen, and W. Z. Yang, Math. Comput. Model. **51**, 1433 (2010).
7. X. Zhang, D. L. Li, W. Z. Yang, J. X. Wang, and S. X. Liu, Sens. Lett. **9**, 1020 (2011).
8. R. L. Long, M. P. Bange, S. G. Gordon, and G. A. Constable, Text. Res. J. **80**, 463 (2010).
9. M. Xu, Opt. Express **12**, 6530 (2004).
10. M. F. G. Wood, X. X. Guo, and I. A. Vitkin, J. Biomed. Opt. **12**, 014029 (2007).
11. H. G. Akarcay, A. Hohmann, A. Kienle, M. Frenz, and J. Ricka, Appl. Opt. **53**, 7576 (2014).
12. T. L. Yun, N. Zeng, W. Li, D. Z. Li, X. Y. Jiang, and H. Ma, Opt. Exp. **17**, 16590 (2009).
13. A. J. Radosevich, J. D. Rogers, I. R. Capoglu, N. N. Mutyal, P. Pradhan, and V. Backman, J. Biomed. Opt. **17**, 115001 (2012).
14. A. Kienle and J. Schafer, Opt. Lett. **37**, 3246 (2012).
15. M. Li, P. Lu, Z. Yu, L. Yan, Z. Chen, C. Yang, and X. Luo, J. Opt. Soc. Am. A Opt. Image Sci. Vis. **30**, 448 (2013).
16. A. Doronin, A. J. Radosevich, V. Backman, and I. Meglinski, J. Opt. Soc. Am. A Opt. Image Sci. Vis. **31**, 2394 (2014).
17. D. Kim and J. Lee, Opt. Lett. **39**, 3378 (2014).
18. M. Jia, S. Cui, X. Chen, M. Liu, X. Zhou, H. Zhao, and F. Gao, Chin. Opt. Lett. **12**, 031702 (2014).
19. C. Gu and P. Yeh, J. Opt. Soc. Am. A Opt. Image Sci. Vis. **10**, 966 (1993).
20. B. Peng, T. H. Ding, and P. Wang, Appl. Opt. **51**, 6325 (2012).
21. E. S. Thomson, L. A. Wilen, and J. S. Wettlaufer, J. Phys.-Condes. Matter. **21**, 195407 (2009).
22. A. Weidlich and A. Wilkie, ACM Trans. Graph. **27**, 1 (2008).
23. P. Yeh, J. Opt. Soc. Am. **69**, 742 (1979).
24. H. M. Guo, X. Y. Weng, G. R. Sui, X. M. Dong, X. M. Gao, and S. L. Zhuang, Opt. Commun. **284**, 5509 (2011).
25. J. Henrie, S. Kellis, S. M. Schultz, and A. Hawkins, Opt. Express **12**, 1464 (2004).
26. G. Sharma, W. C. Wu, and E. N. Daa, Color Res. Appl. **30**, 21 (2005).
27. M. Q. Jia, L. Tong, Y. Chen, Y. Wang, and Y. Z. Zhang, J. Appl. Remote Sens. **7**, 18 (2013).
28. M. H. Sun, H. H. He, N. Zeng, E. Du, Y. H. Guo, S. X. Liu, J. Wu, Y. H. He, and H. Ma, Biomed. Opt. Express **5**, 4223 (2014).
29. S. Alali and A. Vitkin, J. Biomed. Opt. **20**, 061104 (2015).
30. K. Yan, S. Wang, S. Jiang, L. Xue, Y. Song, Z. Yan, and Z. Li, Chin. Opt. Lett. **12**, 092901 (2014).